Coherent frequency up-conversion of microwaves to the optical telecommunications band in an Er:YSO crystal

Xavier Fernandez-Gonzalvo,[1] Yu-Hui Chen,[1] Chunming Yin,[2] Sven Rogge,[2] and Jevon J. Longdell[1]

[1]*The Dodd-Walls Centre for Photonic and Quantum Technologies & Department of Physics, University of Otago, 730 Cumberland Street, Dunedin, New Zealand*

[2]*Centre of Excellence for Quantum Computation and Communication Technology, School of Physics, University of New South Wales, Sydney, New South Wales 2052, Australia*

The ability to convert quantum states from microwave photons to optical photons is important for hybrid system approaches to quantum information processing. We report the up-conversion of a microwave signal into the optical telecommunications wavelength band using erbium dopants in a yttrium orthosilicate crystal via stimulated Raman scattering. The microwaves were applied to the sample using a three-dimensional copper loop-gap resonator and the coupling and signal optical fields were single passed. The conversion efficiency was low, in agreement with a theoretical analysis, but can be significantly enhanced with an optical resonator.

I. INTRODUCTION

Superconducting qubits are a rapidly advancing part of quantum information science. The ability to reach deep into the strong-coupling regime of cavity QED using microwaves has revolutionized quantum optics in the microwave regime [1–4], and allows the coupling between superconducting qubits and a broad range of microwave frequency quantum systems [5,6]. The distribution and storage of microwave quantum states, however, present difficult challenges. A way around this problem would be to convert quantum states of microwave photons into optical photons and vice versa. This would allow long-distance propagation of quantum states between superconducting qubit nodes using optical fibers, and it would also allow for quantum memories for light to be used [7–11], which are currently more developed than their microwave counterparts [12–15]. Quantum frequency conversion has been achieved between optical frequencies [16–20] and recently between microwave frequencies [21]. However, so far, quantum frequency conversion from the microwave to the optical domain remains an unsolved challenge.

There are a number of approaches being investigated for the up-conversion process. Optomechanical approaches [22–26] currently have the highest reported efficiencies and can achieve MHz bandwidths. In such approaches, both an optical and a microwave resonator are parametrically coupled through a micromechanical resonator. In order to have quiet frequency conversion, this rather low-frequency intermediate mechanical resonator needs to be cooled to its quantum ground state, and this is currently challenging. Another approach is to use conventional nonlinear optical materials to make resonantly enhanced modulators [27–29].

Two recent proposals [30,31] have suggested using rare-earth-doped solids, with a particular focus on erbium-doped yttrium orthosilicate (Er:YSO). Er:YSO has many attractive features for frequency up-conversion: it has narrow inhomogeneous and homogeneous linewidths for its $^4I_{15/2} \leftrightarrow \,^4I_{13/2}$ optical transition [32], and the wavelength of this transition is in the telecommunications band, where propagation losses in optical fibers are minimized. Because Er^{3+} is a Kramer's ion (odd number of $4f$ electrons), for the nuclear spin free

isotopes (all but ^{167}Er), the ground state is doubly degenerate. It also has rather large effective g values [33,34], such that microwave frequency splittings can be achieved with only modest magnetic fields.

In this paper, we report on single sideband up-conversion of a microwave signal into the optical telecommunications band using rare-earth ion dopants in a crystal, by performing microwave Raman heterodyne spectroscopy in Er:YSO. Raman heterodyne spectroscopy with radio frequency (ca. 0–200 MHz) is a commonly used technique for nuclear spins in rare-earth dopants [35–39]. It has also been demonstrated in the microwave regime in ruby [40,41] and metalloproteins [42]. These systems, however, are not as attractive for the realization of quantum frequency conversion because they exhibit much broader optical lines.

II. FREQUENCY UP-CONVERSION

Raman heterodyne spectroscopy uses the three-wave mixing that occurs from three energy levels in a Δ configuration, as shown in Fig. 1. To enhance the efficiency of the process, we use a microwave resonator for the lowest-frequency field. The $^4I_{15/2}$ ground state of Er:YSO is Zeeman split under the presence of an applied magnetic field $\vec{B}$, making the $|1\rangle \leftrightarrow |2\rangle$ transition resonant with the microwave cavity. When the input microwave field Ω_μ is applied, it generates a coherence between levels $|1\rangle$ and $|2\rangle$. Simultaneously, the optical coupling field Ω_ξ drives a second coherence between levels $|2\rangle$ and $|3\rangle$. The presence of these two coherences generates a third one between levels $|1\rangle$ and $|3\rangle$, which gives an output signal field Ω_S at a frequency equal to the sum of the frequencies of the microwave and the coupling fields. As long as the sample is small compared to the wavelength of the microwave field, the signal field will be generated in the same spatial mode as the coupling beam. The signal field can then be readily detected in a photodiode as a heterodyne beat note on the coupling beam.

By looking at Fig. 1, one can see that the $|2\rangle \leftrightarrow |3\rangle$ optical coupling field is not the only option that will allow frequency conversion. In reality, there are four
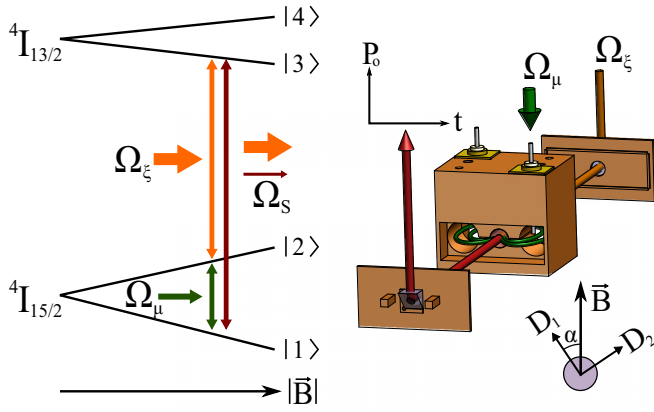
FIG. 1. (Color online) Left: The $^4I_{15/2}$ and $^4I_{13/2}$ levels in Er:YSO are Zeeman split under the presence of an external magnetic field $\vec{B}$. The Raman heterodyne signal is produced when a microwave field Ω_μ and an optical field Ω_ξ drive two transitions in a three-level atom. A coherence is produced on the third transition which generates an optical signal field Ω_S. This can be detected as a beat note on the optical drive field, i.e., a modulation in the optical output power P_o at the same frequency as the microwave field. Right: Depiction of the experimental setup. A copper loop-gap resonator holds an Er:YSO sample inside. Light is coupled in and out using a pair of prisms. Microwaves are coupled via two straight antennas. The green loops inside the resonator represent the microwave magnetic field lines. The external magnetic field is applied in the vertical direction, parallel to the D_1-D_2 plane of the crystal, at an angle α as measured from D_1.

possibilities for the coupling and the converted light frequencies, while keeping the input microwaves at the $|1\rangle \leftrightarrow |2\rangle$ transition: coupling $|2\rangle \leftrightarrow |3\rangle(|2\rangle \leftrightarrow |4\rangle)$ and converted signal $|1\rangle \leftrightarrow |3\rangle(|1\rangle \leftrightarrow |4\rangle)$, and the vice-versa cases with coupling $|1\rangle \leftrightarrow |3\rangle(|1\rangle \leftrightarrow |4\rangle)$ and converted signal $|2\rangle \leftrightarrow |3\rangle(|2\rangle \leftrightarrow |4\rangle)$. For the cases in which the coupling field starts from $|2\rangle$, only pure conversion is achieved. For the cases where the coupling field starts from $|1\rangle$, parametric gain can also be present. As it will be shown later in the experimental results, however, parametric gain is negligible in our experiment since the optical depth of our sample is small. All of the measurements presented in Sec. III are performed in a configuration such as that presented in Fig. 1.

A. Experimental realization

The crystalline structure of YSO belongs to the C_{2h}^6 symmetry group, with two crystallographically inequivalent sites where erbium can replace yttrium. In this work, we focused on Site 1 with a transition wavelength of $\lambda_1 = 1536.478$ nm [43]. YSO has three orthogonal optical extinction axes: D_1, D_2, and b. We use a cylindrical Er:YSO sample of 4.95 mm diameter by 12 mm length, with an erbium number concentration of 0.001%. The optical b axis of the crystal is aligned along the length of the cylinder, and so the D_1-D_2 plane is parallel to the end faces. The sample sits inside a copper three-dimensional loop-gap microwave resonator, with a resonant frequency of 4.9 GHz and a linewidth of 16 MHz (quality factor $Q \simeq 300$). This kind of resonator provides very good filling factors ($\sim$0.8) and makes optical coupling to the sample a simple task, since two optical windows can be opened in the end caps at a null

point of the surface currents, thus not affecting the properties of the cavity very much. Input and output microwave powers are coupled with a pair of straight antennas inside the cavity space. The input light, at 1536 nm, is coupled into and out of the sample with the aid of a pair of coupling prisms, and fiber-coupled collimators. The input fiber is a single-mode fiber, while for the output one we use a multimode fiber for ease of coupling. A superconducting magnet generates a magnetic field perpendicular to the longitudinal direction of the sample (i.e., in the $D1$-$D2$ plane) between 0 and 300 mT. The angle α, measured from D_1 to $\vec{B}$, can be varied by rotating the sample. A more detailed explanation of the complete experimental setup can be found in Appendix C.

The strength for each of the optical transitions in Fig. 1 is given by the product of the electronic transition dipole moment and the overlap of the two spin states. This overlap is calculated by diagonalizing the spin Hamiltonian [33] and taking the inner product of the respective eigenstates. The orientation of the magnetic field has to be chosen carefully, so as to maximize the difference between the quantization axes for the ground and excited states and thus allow Δ transitions. For the situation in which $\vec{B}$ is contained in the D_1-D_2 plane, the calculated angle that maximizes the overlap between states $|2\rangle$ and $|3\rangle$ is $\alpha_M = 29°$.

After the frequency conversion process, the ac component of the heterodyne signal detected in the photodiode is high-pass filtered and amplified, and sent into a rf spectrum analyzer. An inconvenient consequence of using a multimode fiber for the output light is that there is loss in the modulation due to dephasing of the different propagation modes. In our setup, this loss is typically from 3 to 10 dB, and it depends on the arrangement of the fiber. From the power detected by the spectrum analyzer, we can work out the optical power of the generated signal sideband P_S.

B. Raman heterodyne spectroscopy

Our Raman heterodyne spectroscopy results are presented in the color plot of Fig. 2. The power of the generated signal field is measured as we scan the magnetic field and the coupling laser frequency f_ξ. On the left side, in white, we plot an optical absorption spectrum for $|\vec{B}| = 0$ (dotted line) and for $|\vec{B}| = 0.178$ T (solid line). Note that due to various etalon effects, the background of these measurements is not constant. In the optical absorption spectrum for $|\vec{B}| = 0.178$ T, the four optical transitions can be observed. The strong ones ($|1\rangle \leftrightarrow |3\rangle$ and $|2\rangle \leftrightarrow |4\rangle$) appear as peaks around $\Delta f_\xi = \pm 1.6$ GHz, while the weak ones ($|1\rangle \leftrightarrow |4\rangle$ and $|2\rangle \leftrightarrow |3\rangle$) appear as smaller shoulders at about $\Delta f_\xi = \pm 3.4$ GHz. The ratio between the absorption level of the weak and the strong lines is close to the expected value for $\alpha \simeq \alpha_M$. From the absorption measurements, we can also extract an inhomogeneous broadening of the optical transition of $\sim$2.5 GHz FWHM. Comparing the Raman heterodyne spectroscopy data with the absorption spectrum at $|\vec{B}| = 0.178$ T, we see that the four main peaks in the color plot (in red) coincide with the absorption on each of the lines, as is to be expected. It can also be seen that the peak signal is slightly higher for the lowest-frequency peaks, which can be explained using hole-burning arguments.
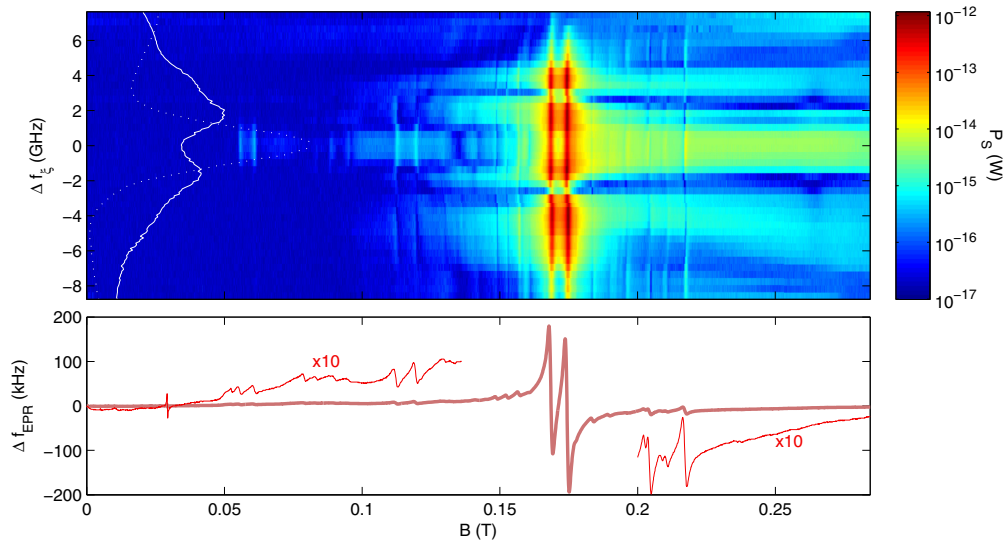
FIG. 2. (Color online) Top: Raman heterodyne spectroscopy on Er:YSO, showing frequency conversion from microwave to optical telecom frequencies. The strength of the magnetic field is plotted in the horizontal axis, and the coupling laser detuning is plotted on the vertical axis. The color scale indicates the power of the output signal field. On the left, the white dotted line represents the optical absorption spectrum for $|\vec{B}| = 0$. The solid white line corresponds to the optical absorption spectrum for $|\vec{B}| = 0.178$ T. Bottom: EPR spectrum of the Er:YSO sample. The regions away from the main peaks have been magnified for clarity. In both plots, the presence of double peaks along the horizontal axis is due to misalignment in the magnetic field, breaking the magnetic degeneracy of the two inequivalent orientations of Er^{+3} in YSO.

C. Electron paramagnetic resonance

Beneath the Raman heterodyne spectroscopy data is the electron paramagnetic resonance (EPR) spectrum of our sample. To take these EPR measurements, we apply a frequency-modulated (FM) microwave signal into the input port of the microwave cavity and monitor the transmitted intensity using a lock-in amplifier. In this way, we are able monitor the resonant frequency shift of our cavity (Δf_{EPR}) as is done in Pound frequency locking [44]. As the spin transitions are swept through resonance with the cavity, they pull the resonator frequency first one way and then the other, resulting in dispersive-shaped peaks. The collection of vertical lines in the Raman heterodyne spectrum and the smaller peaks in the EPR spectrum are due to the ^{167}Er isotope, which has nonzero nuclear spin ($I = 7/2$) and therefore exhibits hyperfine splitting even for $|\vec{B}| = 0$.

The EPR data presented in Fig. 2 shows a maximum frequency shift of around 180 kHz. The measurements shown in the figure are taken for an input microwave power of 0 dBm, which is enough to start to saturate the microwave transition in the absence of the optical field. For saturation-free measurements, at lower microwave powers, we get a maximum shift of around 260 kHz, which agrees with our numerical simulations. From this EPR shift, we can extract a cavity-atom cooperativity factor of the order of 6×10^{-2}.

Comparing the Raman heterodyne and the EPR spectra, we can see that most of the features present in the Raman heterodyne spectroscopy data are also replicated in the EPR data. We assign the EPR peak present at $B \approx 0.03$ T to the Er atoms in Site 2 of YSO. Because the optical transition for these atoms is at a different wavelength, we do not see a signal in Raman heterodyne spectroscopy.

III. CHARACTERIZATION OF THE CONVERSION PROCESS

In this section, we characterize the conversion process by examining the dependency of the output signal power with the input microwave and coupling powers. We compare these measurements with a numerical model of our experiment, which we also use to find the various losses in our setup. Finally, we estimate the efficiency of the conversion process and discuss several ways by which it can be increased.

A. Scaling with the input powers

Figure 3 shows, in red, the dependence of the signal field power with the input microwave power P_μ and the detected coupling laser power P_ξ. The laser coupling power is measured at the output of the system, and is not corrected for optical losses between the sample and the power meter. In blue, we plot a fitted curve for these measurements based on our theoretical model, briefly discussed in Sec. III B. The dependency of P_S with P_μ follows the expected pattern for a three-wave mixing process: it increases linearly until it reaches a saturation point, in our case around $P_\mu = 20$ dBm. These measurements are taken for $P_\xi = 1.8$ mW.

The dependency of P_S with P_ξ, however, does not follow a linear relation for large laser powers. The faster-than-linear rate at which the signal increases with the pump laser power is due to optical pumping improving the population difference between the two $I_{15/2}$ sublevels, lowering the effective spin temperature. This fact is particularly convenient since, for a low noise conversion process, the spins temperature will need to be small compared with the frequency of the input microwave field. These measurements are taken for an input microwave power $P_\mu = 0$ dBm.
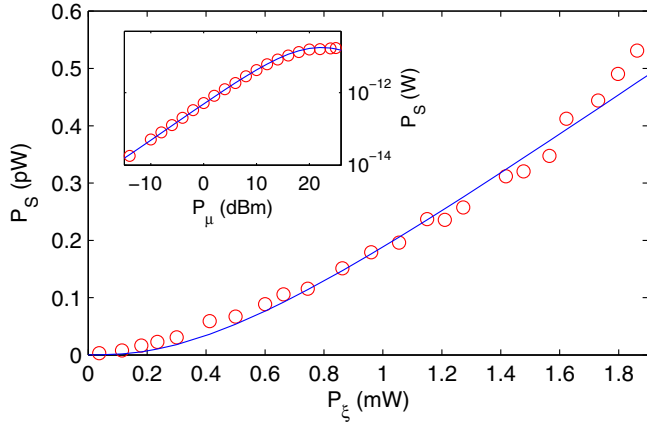
FIG. 3. (Color online) Signal power as a function of detected coupling laser power (main figure) and input microwave power (inset) in red, along with the corresponding theoretical modeling in blue. The faster-than-linear growth of P_S vs P_ξ shows optical cooling of the spins via optical pumping.

B. Numerical model and propagation losses

To model the experiment and plot the blue lines in Fig. 3, we treat each erbium atom as a three-level system and use standard master equation techniques. This is described in detail in Appendix B. The optical and spin dephasing times are not known precisely and are allowed to vary, as is the spin lifetime. In the fitting process, we also introduce two free parameters ζ_μ and ζ_ξ^{-1}, which take into account the propagation losses of P_μ from the setup input to the microwave cavity and the inverse loss of P_ξ from the photodiode detector to the sample. The fitted values for these loss and inverse loss parameters are $\zeta_\mu = 13.1$ dB and $\zeta_\xi^{-1} = -6.4$ dB. It is hard to compare these two numbers with the measured losses of the setup. Some of them are temperature dependent, and it is hard to quantify them at low temperatures for practical reasons, as this would require one to include optical and microwave detectors inside the cryogenic apparatus at 4 K. The measured ζ_μ at room temperature is about 8 dB. In the regime where P_S is proportional to P_μ, the loss of heterodyne signal in the multimode fiber is equivalent to a loss in microwave power. This multimode fiber loss is measured to be between 3 and 10 dB, depending on the geometrical arrangement of the fiber. To these two numbers, we have to add the effects of lowering the temperature in the coaxial microwave wires, which are unknown but can be expected to be of the order of a few dB. For the optical losses, we can measure the loss from the sample to the detector at room temperature, and it is around 5 dB. It is hard to make an estimation of how lowering the temperature will modify this number. We could observe a total decrease in transmitted power of -10 dB through our complete optical setup after the system was cold, but this number takes into account both input and output losses, which we cannot measure separately with the system inside the cryostat. All in all, we consider our fitted loss parameters to be in reasonable agreement with our observations.

C. Conversion efficiency

By comparing the input and the signal field powers, we can calculate a number conversion efficiency $\eta_n = \frac{P_S}{P_\mu} \cdot \frac{f_\mu}{f_\xi}$,

where f_μ is the input microwave frequency. This efficiency η_n accounts for the fraction of microwave photons converted into optical telecom photons. For a coupling power of ~ 2 mW and making the appropriate corrections for ζ_μ and ζ_ξ^{-1}, we get a conversion efficiency of $O(10^{-12})$. In order to get closer to the target of unity conversion efficiency, the most important improvement will be to add a doubly resonant optical cavity (for the coupling and signal fields), which will improve the efficiency by a factor proportional to the finesse of the cavity squared F^2, where F can be as high as $O(10^5)$. On top of this effect, cavity enhancement of the coupling field should increase the effectiveness of the optical cooling of the spins, additionally increasing the efficiency of the conversion process. There are also numerous other improvements that can be made. A more homogeneous magnetic field is very desirable, since it would reduce the microwave inhomogeneous linewidth. The optical depth used in this experiment is also rather low (0.02 mm^{-1}). Much larger optical depths have been observed in Er:YSO without the penalty of broader inhomogeneous lines [45]. Astonishingly narrow absorption lines with good optical depth have also been reported for erbium dopants in isotopically pure yttrium lithium fluoride [46]. The Q factor of ~ 300 for our microwave resonator is also rather modest, as the cavity is strongly overcoupled in our experiment. Using similar resonators weakly coupled to the input and output antennas, we are able to achieve intrinsic Q factors of around 6×10^3, and we believe even higher values are possible.

IV. CONCLUSIONS

In summary, we have presented a different way to convert microwave signals into the optical telecommunications band by means of a cryogenically cooled rare-earth sample inside a three-dimensional microwave cavity. We have fitted our heterodyne spectroscopy experimental results using a theoretical model, obtaining realistic values for the different variable parameters involved in the calculations. Finally, although the efficiency of this initial demonstration is low, there are many ways to improve it, the most significant of which is enhancing the effect of the two optical fields with an optical resonator. Among possible designs for this optical resonator is the Fabry-Perot resonator as proposed in [30] or a whispering-gallery-mode-type resonator as investigated in [28].

APPENDIX A: A NOTE ON COHERENCE

While we have not performed any direct measurement of phase preservation in the up-conversion process, we can be certain that this process is a coherent one. The observed heterodyne peaks are a few tens of Hz wide. Both the optical
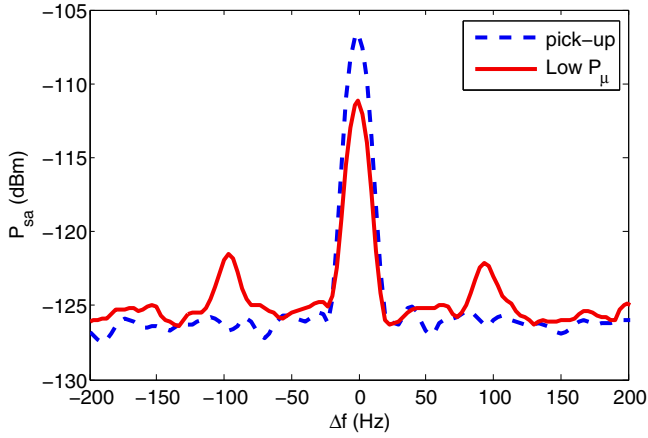
FIG. 4. (Color online) Heterodyne signal as measured by the spectrum analyzer, showing interference between the generated signal and the pick-up noise from the signal generator. The sidebands are attributed to sidebands in the laser frequency due to mechanical vibrations in the laser box.

and the microwave transitions in Er:YSO are much wider than that, and hence the only explanation is that this signal is indeed generated in a Raman scattering process, which is inherently coherent. In other words, the only process in our sample that can generate such a narrow signal is a coherent process. In addition, we are performing heterodyne detection, so our measurements are only sensitive to that light which is coherent with the pump beam.

To further support this claim, there is the following experimental observation, represented in Fig. 4. When measuring the Raman heterodyne signal with the spectrum analyzer, the noise background is not flat. Instead, we can observe a small peak at the signal generator's output frequency. This is pick-up noise coming directly from the signal generator's oscillator to the analyzer (and the amplifier preceding it), and it is present even when the output of the signal generator is shut down (but the oscillator inside the signal generator is still on) or the optical detector is blocked. When measuring the heterodyne signal power versus the input microwave power, for high microwave powers, the heterodyne signal is much bigger than the pick-up noise, and the latter one can be neglected. For low microwave powers, however, the detected peak becomes smaller than the pick-up noise alone. This means that the detected signal and the pick-up noise interfere destructively, which in turn means they are coherent with each other. It is safe to assume that the pick-up noise will be coherent with the signal coming out of the signal generator since they come from the same source, so we can conclude that the converted signal is coherent with the input microwave signal, and therefore so is the conversion process.

APPENDIX B: THEORETICAL MODEL

To model the experiment and plot the blue lines in Fig. 3, we treat each erbium atom as a three-level atom driven by a microwave field which connects the two lowest states $|1\rangle$ and $|2\rangle$, and an optical pump field which connects states $|2\rangle$ and $|3\rangle$. In the interaction picture, we have the following Hamiltonian

for a single atom:

$$H = \delta_2 \sigma_{22} + \delta_3 \sigma_{33} + \Omega_\mu(\vec{r})(\sigma_{12} + \sigma_{21}) + \Omega_\xi(\vec{r})(\sigma_{23} + \sigma_{32}), \quad \text{(B1)}$$

where δ_2 is the detuning from the microwave cavity frequency, δ_3 is the detuning from the coupling laser frequency, and $\sigma_{ij} = |i\rangle\langle j|$. Because in the center of the loop-gap resonator the magnetic field is rather uniform, we can take the microwave Rabi frequency to be a constant, $\Omega_\mu(\vec{r}) \Rightarrow \Omega_\mu$. We take the optical pump field as a plane wave propagating along the z axis so the resulting Rabi frequency, which satisfies $\Omega_\xi(\vec{r}) \equiv \Omega_\xi \cdot e^{ink_{32}z}$, is represented by a traveling wave along the z axis, where k_{32} is the wave vector for light resonant with the $|2\rangle \leftrightarrow |3\rangle$ transition.

The dynamics of each of the atoms is governed by the master equation

$$\dot{\rho} = -i[\rho, H] + \mathcal{L}_{\text{loss}}\rho, \quad \text{(B2)}$$

where ρ is the density operator of a single atom and $\mathcal{L}_{\text{loss}}$ is the loss Lindblad superoperator. Contributing to $\mathcal{L}_{\text{loss}}$ are the collapse operators [47] describing the following: the spontaneous emissions from state $|3\rangle$ to states $|1\rangle$ and $|2\rangle$ ($\sqrt{\gamma_{31}}\sigma_{31}$, $\sqrt{\gamma_{32}}\sigma_{32}$); spin lattice relaxation between states $|1\rangle$ and $|2\rangle$ ($(N_b + 1)\sqrt{\gamma_{21}}\sigma_{12}$, $N_b\sqrt{\gamma_{21}}\sigma_{21}$); and the dephasings for the microwave and optical transitions ($\sqrt{\gamma_{2d}}\sigma_{22}$, $\sqrt{\gamma_{3d}}\sigma_{33}$). Here, $N_b = (e^{\hbar\omega/(kT)} - 1)^{-1}$ is the mean number of bath quanta at the microwave frequency. For our situation, with a 5 GHz microwave frequency and a 4.2 K temperature, $N_b \approx 17$.

The steady-state coherence on the $|3\rangle \leftrightarrow |1\rangle$ transition is given by $\rho_{31}(\delta_2, \delta_3)$, and it can be obtained from the steady-state solution of Eq. (B2). Then, the total polarization at a given position z and at the $|3\rangle \leftrightarrow |1\rangle$ frequency will be given by

$$P(z) = N d_{13} \iint d\delta_2\, d\delta_3\, g(\delta_2, \delta_3)\rho_{31}(\delta_2, \delta_3, z) + \text{c.c.}, \quad \text{(B3)}$$

where N is the density of atoms, d_{ij} is the electric dipole moment of the transition between $|i\rangle$ and $|j\rangle$, and $g(\delta_2, \delta_3)$ describes the distribution of the microwave (δ_2) and optical (δ_3) detunings due to inhomogeneous broadening, normalized so that $\iint d\delta_2 d\delta_3\, g(\delta_2, \delta_3) = 1$. In our calculations, $g(\delta_2, \delta_3)$ is assumed to be a two-dimensional Gaussian function with standard deviations Δ_μ and Δ_o.

This $P(\vec{r})$ acts as a source term and generates a sideband signal via

$$\frac{\partial E_S(z)}{\partial z} = \frac{i\mu_0 \omega_{31} c}{2n} P(z), \quad \text{(B4)}$$

where ω_{31} is the angular frequency of the $|3\rangle \leftrightarrow |1\rangle$ transition, n is the refractive index of the sample, and μ_0 and c are the magnetic permeability and the speed of light in the vacuum, respectively. In the optically thin limit, this differential equation is trivial to solve and the result can be rearranged to give

$$|E_S(z = L)| = \frac{\alpha_{31}L}{2} \cdot \frac{d_{23}}{d_{13}} \cdot \frac{I}{\pi\Omega_\xi} \cdot \mathbf{Re}\left(\frac{\int_0^L e^{ink_\mu z}\, dz}{L}\right) \cdot E_\xi, \quad \text{(B5)}$$

where α_{31} is the absorption coefficient for the $|1\rangle \leftrightarrow |3\rangle$ transition, L is the length of the sample, E_ξ is the amplitude of the coupling laser beam, and $I = \sqrt{2\pi}\,\Delta_o \iint d\delta_2\, d\delta_3\, g(\delta_2, 0)\rho_{31}(\delta_2, \delta_3, z = 0)$. The first and the second terms on the right-hand side of Eq. (B5) can be easily obtained from experimental absorption measurements for the different transitions. The fourth term is a phase-matching factor due to the fact that the driving laser has a propagating phase of $e^{ink_{32}z}$, while the sideband signal has a propagation phase of $e^{ink_{31}z}$ (where k_{ij} are the wave vectors for the $|i\rangle \leftrightarrow |j\rangle$ transition), and it can be calculated very accurately. The third term including I is calculated numerically by solving the master equation as explained above.

The spontaneous-emission rates for the two optical transitions used to model the experiment are $\gamma_{31} = 60$ s^{-1} and $\gamma_{32} = 30$ s^{-1}. These are calculated from the known 11 ms excited-state lifetime and the branching ratios expected from the spin Hamiltonians.

The optical inhomogeneous linewidth is taken from the optical absorption measurements ($\Delta_o = 2\pi \times 1$ GHz) and the spin inhomogeneous linewidth is taken from EPR results ($\Delta_\mu = 2\pi \times 13$ MHz).

The dephasing rates and the spin lattice relaxation time are not known for this temperature and magnetic field, so they are allowed to vary and the values that gave the best fit to the data are chosen. These values are $\gamma_{3d} = 2.8 \times 10^6$ s^{-1}, $\gamma_{2d} = 1.7 \times 10^6$ s^{-1}, and $\gamma_{21} = 27.4$ s^{-1} (1 ms lifetime).

We also introduce two free parameters ζ_μ and ζ_ξ^{-1}, which take into account the propagation losses of P_μ from the setup input to the microwave cavity and the inverse loss of P_ξ from the photodiode detector to the sample. The fitted values for these loss and inverse loss parameters are $\zeta_\mu = 13.1$ dB and $\zeta_\xi^{-1} = -6.4$ dB, which are well within the experimental expectations.

APPENDIX C: EXPERIMENTAL SETUP

The setup for our experiment is depicted in Fig. 5. The pump beam is generated by a fiber-coupled external cavity diode laser at 1536 nm, and then amplified by an erbium-doped fiber amplifier. A polarization controller is used to maximize the output heterodyne signal. The pump beam travels through a single-mode fiber and is then collimated using a fiber-coupled graded-index (GRIN) lens collimator. With the help of a couple of right-angle prisms, the beam is sent in and out of the microwave resonator, passing through the Er:YSO sample on its way. The output light, consisting of the pump beam and the up-converted signal, is then coupled into a multimode fiber using a second GRIN lens collimator. At the output of the multimode fiber, the light is collimated into a Hamamatsu G7096-03 photodiode detector. A bias tee and a battery serve
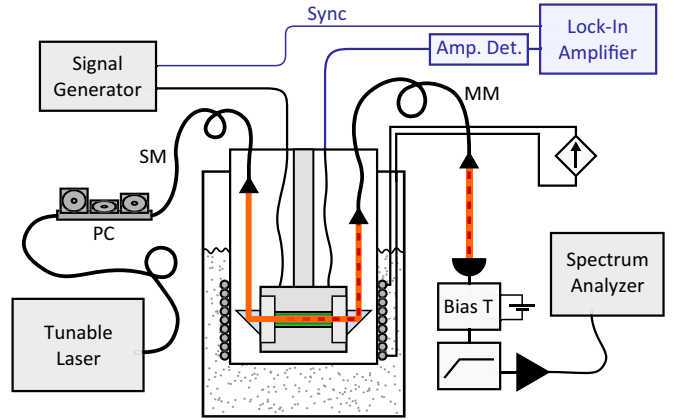

FIG. 5. (Color online) Experimental setup. The part drawn in blue is used for EPR measurements only. PC: polarization controller. SM: single-mode fiber. MM: multimode fiber.

the double purpose of biasing the photodiode and separating the ac from the dc components of the detected signal. The ac component is then high-pass filtered and analyzed with a FieldFox N9916A vector network analyzer working as a spectrum analyzer. To drive the microwave cavity, we use an R&S SMP 22 microwave signal generator. Microwaves are coupled in and out of the cavity using a couple of straight antennas. The cavity itself has a resonant frequency of 4.9 GHz, a loaded Q factor of around 300, and a room-temperature transmission ($|S_{21}|^2$) of around 6 dB.

The resonator and the coupling optics sit inside an encasing stainless-steel tube filled with about one mbar of helium, which acts as a thermal exchange gas. This tube is then inserted into a liquid-helium bath cryostat. In this way, we can avoid optical distortions created by the boiling helium and thermal shocks that could be detrimental to the various optical components. Surrounding the end of the encasing tube is a superconducting magnet powered by a variable current source, which can generate magnetic fields of up to 0.3 T.

The part drawn in blue in Fig. 5 corresponds to the EPR setup, consisting of an amplitude detector and an SRS SR830 lock-in amplifier. In order to do EPR experiments, we add FM modulation to the microwave signal at 3 kHz. When this FM signal passes through the cavity, it gets converted into an AM signal with a modulation amplitude proportional to the slope of the cavity transmission curve. Using an amplitude detector, we can measure this modulation amplitude with a lock-in amplifier, which needs to be synchronized with the FM at the signal generator.

The laser source, the signal generator, the lock-in amplifier, the variable current source powering the magnet, and the spectrum analyzer are all remotely controlled from a computer (not shown in the figure).

[1] Y. Kubo, F. R. Ong, P. Bertet, D. Vion, V. Jacques, D. Zheng, A. Dréau, J.-F. Roch, A. Auffeves, F. Jelezko *et al.*, Phys. Rev. Lett. **105**, 140502 (2010).

[2] D. I. Schuster, A. P. Sears, E. Ginossar, L. DiCarlo, L. Frunzio, J. J. L. Morton, H. Wu, G. A. D. Briggs, B. B. Buckley, D. D. Awschalom *et al.*, Phys. Rev. Lett. **105**, 140501 (2010).

[3] J. D. Teufel, D. Li, M. S. Allman, K. Cicak, A. J. Sirois, J. D. Whittaker, and R. W. Simmonds, Nature (London) **471**, 204 (2011).

[4] S. Probst, H. Rotzinger, S. Wünsch, P. Jung, M. Jerger, M. Siegel, A. V. Ustinov, and P. A. Bushev, Phys. Rev. Lett. **110**, 157001 (2013).

[5] M. D. LaHaye, J. Suh, P. M. Echternach, K. C. Schwab, and M. L. Roukes, Nature (London) **459**, 960 (2009).

[6] X. Zhu, S. Saito, A. Kemp, K. Kakuyanagi, S.-i. Karimoto, H. Nakano, W. J. Munro, Y. Tokura, M. S. Everitt, K. Nemoto *et al.*, Nature (London) **478**, 221 (2011).

[7] J. J. Longdell, E. Fraval, M. J. Sellars, and N. B. Manson, Phys. Rev. Lett. **95**, 063601 (2005).

[8] M. Hosseini, B. M. Sparkes, G. Hetet, J. J. Longdell, P. K. Lam, and B. C. Buchler, Nature (London) **461**, 241 (2009).

[9] I. Usmani, M. Afzelius, H. de Riedmatten, and N. Gisin, Nat. Commun. **1**, 12 (2010).

[10] M. P. Hedges, J. J. Longdell, Y. Li, and M. J. Sellars, Nature (London) **465**, 1052 (2010).

[11] N. Timoney, I. Usmani, P. Jobez, M. Afzelius, and N. Gisin, Phys. Rev. A **88**, 022324 (2013).

[12] A. N. Cleland and M. R. Geller, Phys. Rev. Lett. **93**, 070501 (2004).

[13] M. A. Sillanpaa, J. I. Park, and R. W. Simmonds, Nature (London) **449**, 438 (2007).

[14] H. Wu, R. E. George, J. H. Wesenberg, K. Mølmer, D. I. Schuster, R. J. Schoelkopf, K. M. Itoh, A. Ardavan, J. J. L. Morton, and G. A. D. Briggs, Phys. Rev. Lett. **105**, 140503 (2010).

[15] N. Timoney, I. Baumgart, M. Johanning, A. F. Varon, M. B. Plenio, A. Retzker, and C. Wunderlich, Nature (London) **476**, 185 (2011).

[16] S. Tanzilli, W. Tittel, M. Halder, O. Alibart, P. Baldi, N. Gisin, and H. Zbinden, Nature (London) **437**, 116 (2005).

[17] H. J. McGuinness, M. G. Raymer, C. J. McKinstrie, and S. Radic, Phys. Rev. Lett. **105**, 093604 (2010).

[18] A. G. Radnaev, Y. O. Dudin, R. Zhao, H. H. Jen, S. D. Jenkins, A. Kuzmich, and T. A. B. Kennedy, Nat. Phys. **6**, 894 (2010).

[19] S. Zaske, A. Lenhard, C. Keßler, J. Kettler, C. Hepp, C. Arend, R. Albrecht, W.-M. Schulz, M. Jetter, P. Michler *et al.*, Phys. Rev. Lett. **109**, 147404 (2012).

[20] B. Albrecht, P. Farrera, X. Fernandez-Gonzalvo, M. Cristiani, and H. de Riedmatten, Nat. Commun. **5**, 3376 (2014).

[21] K. Inomata, K. Koshino, Z. R. Lin, W. D. Oliver, J. S. Tsai, Y. Nakamura, and T. Yamamoto, Phys. Rev. Lett. **113**, 063604 (2014).

[22] A. H. Safavi-Naeini and O. Painter, New J. Phys. **13**, 013017 (2011).

[23] J. T. Hill, A. H. Safavi-Naeini, J. Chan, and O. Painter, Nat. Commun. **3**, 1196 (2012).

[24] S. A. McGee, D. Meiser, C. A. Regal, K. W. Lehnert, and M. J. Holland, Phys. Rev. A **87**, 053818 (2013).

[25] J. Bochmann, A. Vainsencher, D. D. Awschalom, and A. N. Cleland, Nat. Phys. **9**, 712 (2013).

[26] R. W. Andrews, R. W. Peterson, T. P. Purdy, K. Cicak, R. W. Simmonds, C. A. Regal, and K. W. Lehnert, Nat. Phys. **10**, 321 (2014).

[27] V. Ilchenko, A. A. Savchenkov, A. B. Matsko, and L. Maleki, IEEE Photon. Technol. Lett. **14**, 1602 (2002).

[28] D. V. Strekalov, H. G. L. Schwefel, A. A. Savchenkov, A. B. Matsko, L. J. Wang, and N. Yu, Phys. Rev. A **80**, 033810 (2009).

[29] M. Tsang, Phys. Rev. A **81**, 063837 (2010).

[30] L. A. Williamson, Y.-H. Chen, and J. J. Longdell, Phys. Rev. Lett. **113**, 203601 (2014).

[31] C. O'Brien, N. Lauk, S. Blum, G. Morigi, and M. Fleischhauer, Phys. Rev. Lett. **113**, 063603 (2014).

[32] T. Böttger, Y. Sun, C. W. Thiel, and R. L. Cone, Phys. Rev. B **74**, 075107 (2006).

[33] Y. Sun, T. Böttger, C. W. Thiel, and R. L. Cone, Phys. Rev. B **77**, 085124 (2008).

[34] O. Guillot-Noël, Ph. Goldner, Y. L. Du, E. Baldit, P. Monnier, and K. Bencheikh, Phys. Rev. B **74**, 214409 (2006).

[35] J. Mlynek, N. C. Wong, R. G. DeVoe, E. S. Kintzer, and R. G. Brewer, Phys. Rev. Lett. **50**, 993 (1983).

[36] J. J. Longdell, M. J. Sellars, and N. B. Manson, Phys. Rev. B **66**, 035101 (2002).

[37] M. Lovrić, P. Glasenapp, D. Suter, B. Tumino, A. Ferrier, P. Goldner, M. Sabooni, L. Rippe, and S. Kröll, Phys. Rev. B **84**, 104417 (2011).

[38] L. E. Erickson, J. Phys. C **20**, 291 (1987).

[39] J. J. Longdell, A. L. Alexander, and M. J. Sellars, Phys. Rev. B **74**, 195101 (2006).

[40] S. J. Bingham, D. Suter, A. Schweiger, and A. J. Thomson, Chem. Phys. Lett. **266**, 543 (1997).

[41] M. O. Schweika-Kresimon, J. Gutschank, and D. Suter, Phys. Rev. A **66**, 043816 (2002).

[42] S. J. Bingham, B. Brger, J. Gutschank, D. Suter, and A. J. Thomson, J. Biolog. Inorgan. Chem. **5**, 30 (2000).

[43] C. Li, C. Wyon, and R. Moncorgc, IEEE J. Quantum Electron. **28**, 1209 (1992).

[44] R. V. Pound, Rev. Sci. Instrum. **17**, 490 (1946).

[45] J. Dajczgewand, R. Ahlefeldt, T. Böttger, A. Louchet-Chauvet, J.-L. L. Gouët, and T. Chanelière, New J. Phys. **17**, 023031 (2015).

[46] E. Chukalina, M. Popova, S. Korableva, and R. Abdulsabirov, Phys. Lett. A **269**, 348 (2000).

[47] H. J. Carmichael, *Statistical Methods in Quantum Optics 1: Master Equation and Fokker-Planck Equations* (Springer-Verlag, Berlin Heidelberg, 1999).